IEEE Access
Multidisciplinary | Rapid Review | Open Access Journal

Received 6 March 2024, accepted 16 March 2024, date of publication 21 March 2024, date of current version 27 March 2024.

Digital Object Identifier 10.1109/ACCESS.2024.3380411

RESEARCH ARTICLE

A Non-Steady State NMR Effect Based Time-Varying Magnetic Field Measurement Method and Experimental Apparatus

HANG XU[1], HONG MA[1,2], XIAOHU ZENG[2], HUA ZHANG[2], AND JIANG JIN[2]

[1]School of Physics, Huazhong University of Science and Technology, Wuhan 430074, China
[2]School of Electronic Information and Communications, Huazhong University of Science and Technology, Wuhan 430074, China

Corresponding author: Hong Ma (mahong@hust.edu.cn)

This work was supported in part by the National Natural Science Foundation of China, under Grant 10975056, Grant 11475067, and Grant 62071188; in part by the Innovative Research Program of Huazhong University of Science and Technology under Grant 2015ZDTD017 and Grant 2017KFXKJC012; and in part by the Experimental Apparatus Research Project of Wuhan Pulsed High Magnetic Field Center under Grant 2015KF17.

ABSTRACT Accurate measuring magnetic induction intensity is important for some scientific research. In the paper, the conventional nuclear magnetic resonance (NMR) experiment under static magnetic field has been extended to longitudinal time-varying magnetic field (TVMF), and the time domain transient solution of the Bloch equations for spin nuclei exhibits the so-called non-steady state nuclear magnetic resonance (NSS-NMR) phenomenon. Based on the above effect and the precise gyromagnetic ratio of spin nucleus, a new magnetic field measurement method and corresponding experimental apparatus have been developed in longitudinal TVMF environment. The orthogonal dual-coil probe, radio frequency (RF) exciting and receiving hardware, key signal processing algorithms, host computer controlling and analysis software are deeply studied. In order to improve the signal-to-noise ratio of the NSS-NMR signal, the RF signal envelope shaping and the low-frequency pre-emphasis probe matching techniques are designed and verified by the invented circuit-field-nuclear multi-domain joint simulation subassembly (CFN-MDJS) which is integrated in the host computer software. Furthermore, the multi-tone RF excitation signal substituting the bandpass continuous spectrum signal for NSS-NMR experiment is also verified by the CFN-MDJS. The experimental results under longitudinal 50Hz TVMF environment has demonstrated the authentic existence of the NSS-NMR effect and simultaneously verified the effectiveness of the experimental scheme and signal processing algorithms proposed in the paper.

INDEX TERMS Time-varying magnetic field (TVMF), magnetic field measurement, non-steady state nuclear magnetic resonance (NSS-NMR), envelope shaping, low frequency pre-emphasis, circuit-field-nuclear multi-domain joint simulation (CFN-MDJS).

I. INTRODUCTION

Accurate measuring magnetic induction intensity is the basis of some scientific experiment in magnetic field environment. Resonance based magnetic field measurement is an important kind of method [1], [2], including the electron paramagnetic resonance (EPR) method [3], the optical pump magnetic resonance (OPMR) method [4] and the nuclear magnetic resonance (NMR) method [5]. The EPR method is based on the electron resonance effect and may affected by some external interference to deteriorate the measurement accuracy [6], [7]. The OPMR method combines with optical pumping and magnetic resonance and maybe sensitive to environmental fluctuations and noise [8]. The NMR method

The associate editor coordinating the review of this manuscript and approving it for publication was Xuebo Zhang.

is based on the magnetic resonance absorption while the specific frequency RF wave being incident to non-zero magnetic moment nuclei. Because the spin nuclear gyromagnetic ratio (usually using 1H) has already been accurately measured and the relationship between Larmor precession frequency and longitudinal magnetic induction intensity is strictly linear, the current measurement accuracy of the NMR method is as high as 10 ppm [9].

While measuring static magnetic field by the conventional pulsed NMR method, the spin nuclei are excited by RF pulse sequence, the Larmor precession relationship (LPR) and the corresponding Larmor precession frequency of free induction decay (FID) signal are used to inverse the longitudinal magnetic field [10]. Some studies have shown the pulsed magnetic field (PMF) measuring experiments by the above pulsed NMR technology, such as Haase et al. [11], [12]. Chen et al. have proposed another longitudinal time-varying magnetic field measurement scheme which is based on the so called non-steady state nuclear magnetic resonance (NSS-NMR) effect [13], [14], [15]. In 2022, Zeng et al. had performed the NSS-NMR experiment by exciting the spin nuclei with a band-limited white Gauss signal and acquired the weak NSS-NMR signal [16]. In this paper, a set of TVMF measuring apparatus is developed. The experimental results verify the effectiveness of the TVMF measuring scheme and the corresponding apparatus. In the apparatus, the host computer is used to control the NSS-NMR experimental sequence, process the sampled dual-channel signals. Also, an embedded circuit-field-nuclear multi-domain joint simulation software (CFN-MDJS) integrated in the host computer can simulate the entire NSS-NMR procedure and finally obtain NSS-NMR transient waveforms. Using the software, the envelope shaping method and the low frequency pre-emphasis technique which can improve the signal-to-noise ratio (SNR) of the NSS-NMR signal are researched and another kind of NSS-NMR RF exciting signal, the multi-tone RF signal, is also presented and simulated for validation.

The paper is organized in five sections. Section I is the introduction. Section II explains the NSS-NMR effect and principle, and studies several factors affecting the NSS-NMR response. Section III introduces the longitudinal TVMF measurement installation, including the hardware, the key signal processing algorithms, the host computer controlling and processing software and their implementation. The CFN-MDJS component is also integrated in the host-computer software. Section IV introduces the 50Hz sinusoidal TVMF measurement and inversion results, as well as the simulation verification of the SNR improvement techniques in a longitudinal pulsed magnetic field environment, and the feasibility of multi-tone RF exciting signal in NSS-NMR experiment. Section V is the conclusion and prospect of the paper.

II. THE NSS-NMR EFFECT AND AFFECTING FACTORS

A. THE NSS-NMR PRINCIPLE

According to the quantum mechanics, the spin energy levels of nuclei with non-zero magnetic moments will split into more sub-levels in longitudinal static magnetic field environment which is called Zeeman splitting. Generalized, on the condition of longitudinal TVMFs, the spin nuclei will exhibit continuous time-varying energy level splitting with different quantum number. At the time, if a broadband continuous RF magnetic field is applied to the spin nuclei along the orthogonal polarization direction, the ground state nuclei will resonate with the different frequency RF components and then absorb some RF energy to transition to the excited state with continuous energy level difference distribution. After removing the RF excitation magnetic field, the excited state nuclei will fall back to the ground state and radiate the electromagnetic wave with same frequency synchronously. This is the so-called NSS-NMR effect proposed by H. Ma and Y. Hu et al. in 2012. They also deduced the occupation probability of ^{1}H nuclei distributing in the 1/2 state and -1/2 state under TVMF environment [17] and proposed the magnetic susceptibility equation of the nuclei ensemble under excitation of the longitudinal TVMF and the RF magnetic field [18], [19].

Assume the longitudinal TVMF intensity varying-range being from B_{01} to B_{02}, the energy differences between adjacent energy levels of the corresponding nuclei distribute from $\Delta E_1(=\hbar\gamma B_{01})$ to $\Delta E_2(=\hbar\gamma B_{02})$. If the frequency range of the orthogonal polarization RF magnetic field covers $\nu_1 = \gamma B_{01}/2\pi$ to $\nu_2 = \gamma B_{02}/2\pi$, the relationship between the resonance absorption and the induced radiation electromagnetic energy is $h\nu(t) = g_N\mu_N B_0(t)$ at any time t of the longitudinal magnetic field duration, so the instantaneous angular frequency of the NSS-NMR signal is deduced as:

$$\omega(t) = \gamma B_0(t) \tag{1}$$

The above equation indicates that the frequency of the NSS-NMR signal varies with time and its value changes proportionally with the intensity of the longitudinal TVMFs. The NSS-NMR signal is a typical unstable transient signal.

B. THE NSS-NMR BLOCH EQUATION

The Bloch equations, which quantitatively describes the NMR effect in static magnetic field environment from the electrodynamics standpoint, classically depicts the motion pattern of the spin nuclear magnetization [20]. Extending the Bloch equations to the condition of longitudinal TVMF environment and applying the broadband continuous RF excitation to the nuclei ensemble, the corresponding equilibrium magnetization and transverse/longitudinal relaxation time-constant are all time-variables, then the NSS-NMR Bloch equations could be deduced as:

$$\frac{d\vec{M}}{dt} = \gamma\vec{M}\times\vec{B} - (M_x\vec{e}_x + M_y\vec{e}_y)/T_2 - (M_z - M_{z0})\vec{e}_z/T_1 \tag{2}$$

where $\vec{M} = M_x\vec{e}_x + M_y\vec{e}_y + M_z\vec{e}_z$ is the magnetization vector, $\vec{B}(t) = B_1(t)\vec{e}_x + B_0(t)\vec{e}_z$ is the total magnetic field applying to the spin nuclei ensemble which consists of the

longitudinal TVMF $\vec{B}_0(t)$ and the transverse RF magnetic field $\vec{B}_1(t)$, M_{z0} is the equilibrium magnetization under the longitudinal magnetic field $\vec{B}_0(t)$ before the RF magnetic field applied, T_1 and T_2 are the longitudinal and transverse relaxation time-constant varying with the longitudinal magnetic field $\vec{B}_0(t)$ respectively.

According to the Boltzmann distribution in the static magnetic field, the equilibrium magnetization is expressed as:

$$M_{z0} = \frac{N\hbar^2\gamma^2 I(I+1)}{3kT} B_0 = \chi_0 B_0 \tag{3}$$

where N is the nucleus number per unit volume of NMR sample, I is the spin nuclear quantum number, T is the absolute temperature, χ_0 is the static nuclear susceptibility.

Under longitudinal TVMF, the equilibrium magnetization M_{z0} is unstable and varies with the magnetic field. A.Abragam had pointed out that the nonlinear changing of the equilibrium magnetization caused by the TVMF may be ignored when the changing rate of the TVMF meets $\max\left|\gamma\tau\frac{dB_z(t)}{dt}\right| \ll 1$ within the relevant time τ, so the equation $M_{z0} = \chi_0\vec{B}_{z0}(t)$ is established [22]. If the longitudinal TVMF is a pulsed magnetic field with peak value 0.6 T, the nonlinear variation of the longitudinal/transverse relaxation time could be ignored and the relaxation time-constant are approximately fix. Some numerical calculation methods, such as the fourth-order Runge-Kutta method, can be used to solve the NSS-NMR Bloch equations to obtain the magnetization vector of the spin nuclei ensembles.

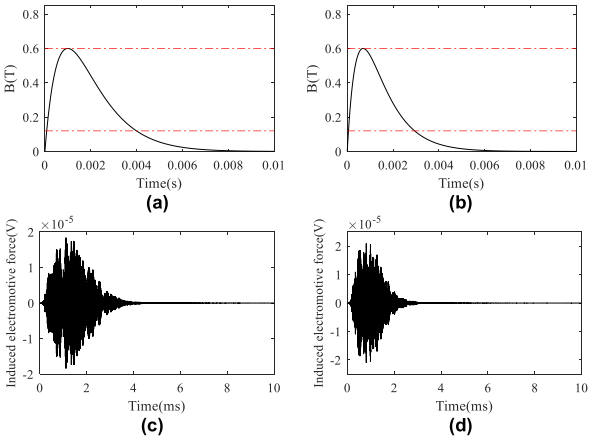

FIGURE 1. Simulation comparisons of the longitudinal TVMF waveform affecting the NSS-NMR signal envelope: (a) The first waveform of the longitudinal pulsed magnetic field with pulse duration 4ms; (b) The second waveform of the longitudinal pulsed magnetic field with pulse duration 3ms; (c) The NSS-NMR signal corresponding to the first longitudinal magnetic field; (d) The NSS-NMR signal corresponding to the second longitudinal magnetic field.

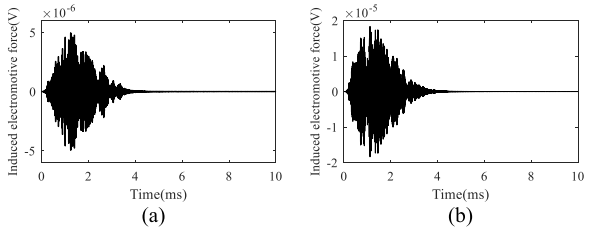

FIGURE 2. Simulation result: (a) The NSS-NMR signal waveform under excitation by a 1W average power RF source; (b) The NSS-NMR signal waveform under excitation by a 10W average power RF source.

C. SOME INFLUENCE FACTORS TO THE NSS-NMR RESPONSE

According to the equation (2), the transverse component $M_y(t)$ of the magnetization vector is related to the longitudinal TVMF $\vec{B}_0(t)$ and the RF exciting magnetic field $\vec{B}_1(t)$. In addition, the relaxation time-constant of the spin nuclei sample varying with the longitudinal magnetic field also affect the NSS-NMR signal. The several affecting factors of the NSS-NMR response can be analyzed by the numerical solution of the NSS-NMR Bloch equations.

1) LONGITUDINAL MAGNETIC FIELD WAVEFORM AFFECTING THE ENVELOPE OF NSS-NMR SIGNAL

Under two kinds of longitudinal TVMF environments with same peak magnetic induction intensity 0.6T and different field durations, the NSS-NMR signals have numerically been calculated respectively by exciting 1H nuclei sample with a bandpass Gaussian RF magnetic field of frequency band covering from 5.1 MHz to 25.5 MHz (corresponding to the field intensity range from 0.12 T to 0.6 T shown as the red dotted curves in Fig. 1(a) and Fig. 1(b)). The NSS-NMR signal waveforms are shown in Fig. 1(c) and Fig. 1(d) which the durations are from 0.1ms to 4.1ms and 0.1ms to 3.4ms, respectively. Furthermore, the rising edge widths and the falling edge widths of the two waveforms are obviously different, the amplitude of initial and end segments of the waveforms are also very low.

2) THE AVERAGE POWER OF RF EXCITATION MAGNETIC FIELD AFFECTING THE AMPLITUDE OF THE NSS-NMR SIGNAL

Theoretically, the amplitude of the NSS-NMR signal is proportional to the average power of the RF excitation magnetic field. When the different RF bandpass Gaussian voltage sources (internal resistance being 50 ohm) with 1 W and 10 W average power are applied to the RF excitation coil of the probe respectively, the calculated NSS-NMR signals are shown in Fig. 2(a) and (b) under the longitudinal pulse magnetic field environment depicted in Fig. 1(a).

In the duration of the NSS-NMR signal from 0.1ms to 4.1ms, the peak amplitude ratio of the two NSS-NMR signals is about 3.2 which approximately equals to the average power ratio of the two RF excitation signals.

3) THE SPIN NUCLEI ENSEMBLES SATURATION AND RELAXATION AFFECTING THE NSS-NMR SIGNAL

On the condition of RF continuous wave excitation, the nuclei number distributing on each energy level eventually tends to be consistent and the nuclei sample will not absorb the RF excitation energy and finally reach saturation state. On the other hand, the spin nuclear ensemble can exchange energy

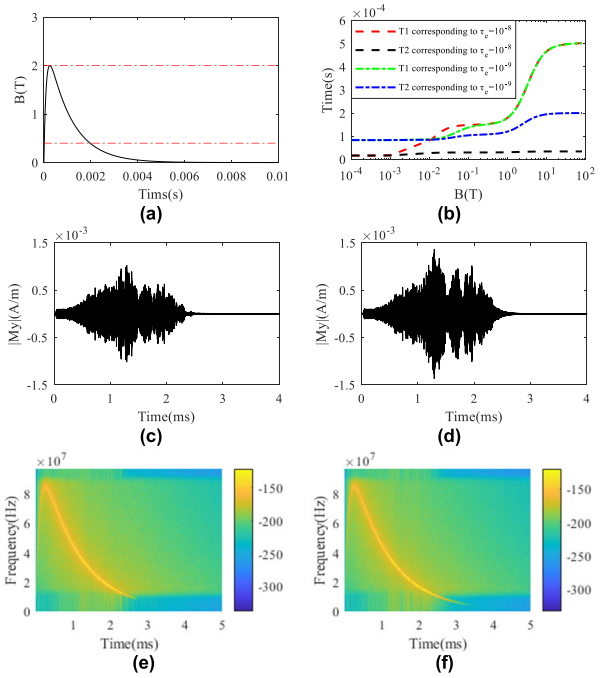

FIGURE 3. Simulation results: (a) The waveform of the longitudinal pulsed magnetic field; (b) Two kinds of relaxation time characteristics varying with the longitudinal magnetic field; (c) The waveform of magnetization component M_y in the first sample; (d) The waveform of magnetization component M_y in the second sample; (e) The time-frequency diagram of M_y in the first sample; (f) The time-frequency diagram of M_y in the second sample.

with the surrounding environment (i.e., spin lattice relaxation effect). Research shows that reduction the spin lattice relaxation effect could reduce the nuclei transition probability and avoid ensemble saturation. Therefore, some paramagnetic ions (such as Cu^{2+}, Gd^{3+}) are usually added into aqueous solution to improve the relaxation rate $R = 1/T_1$ in NMR experiment.

Under the longitudinal TVMF environment, the longitudinal and transverse relaxation time-constant, T_1 and T_2, are no longer constant. In the paper, the Solomon-Bloembergen-Morgan (SBM) formula is adopted to approximately describe the relationship among the relaxation times and the paramagnetic ion species, concentration and longitudinal magnetic field intensity B_0 for the NSS-NMR numerical calculation [23].

$$\frac{1}{T_1} = K_1[\frac{3\tau_c}{1+\gamma_I^2 B_0^2 \tau_c^2} + \frac{7\tau_c}{1+\gamma_S^2 B_0^2 \tau_c^2}] + K_2[\frac{\tau_e}{1+\gamma_S^2 B_0^2 \tau_c^2}] \tag{4}$$

$$\frac{1}{T_2} = \frac{K_1}{2}[4\tau_c + \frac{3\tau_c}{1+\gamma_I^2 B_0^2 \tau_c^2} + \frac{13\tau_c}{1+\gamma_S^2 B_0^2 \tau_c^2}] + \frac{K_2}{2}[\tau_e + \frac{\tau_e}{1+\gamma_S^2 B_0^2 \tau_e^2}] \tag{5}$$

where γ_I and γ_S are the gyromagnetic ratio of protons and electrons, respectively. K_1 and K_2 are the constant coefficients which relate to the paramagnetic solution characteristics such as paramagnetic ion species, concentration, coordination number and proton-ion nuclear distance. τ_c and τ_e are the relevant times for dipole-dipole and spin-spin interactions, respectively.

Fig. 3 shows two NSS-NMR Bloch equations transient solutions and time-frequency diagrams of two kinds of paramagnetic aqueous solution samples with two different relaxation properties while excited by the longitudinal pulsed magnetic field of 2T peak field intensity and faster field variation. The spin-spin correlation time of the two samples are $\tau_e = 10^{-8}$ s and $\tau_e = 10^{-9}$ s, respectively, and other relaxation characteristic parameters are $K_1 = 3.33 \times 10^{13}$, $K_2 = 5.33 \times 10^{12}$, $\tau_c = 2 \times 10^{-11}$ s.

As comparison, Fig. 4 shows the NSS-NMR responses of the two samples excited by a longitudinal 50 Hz sinusoidal TVMF which the amplitude ranges from 0.576T to 0.582T.

The longitudinal relaxation characteristics of the above two samples are similar, but the transverse relaxation time-constant of the first sample is significantly shorter than the second sample, so the amplitude of the former NSS-NMR response is lower and the rising edge of the time-frequency diagram is slightly clearer than the latter in the pulsed magnetic field. However, the clarity and integrity of the falling edge of the time-frequency curve are significantly worse than the latter in the duration of low change rate longitudinal magnetic field. The above phenomenon is more obvious under the 50 Hz sinusoidal magnetic field which the change rate of the longitudinal magnetic field is lower than that of the pulsed magnetic field.

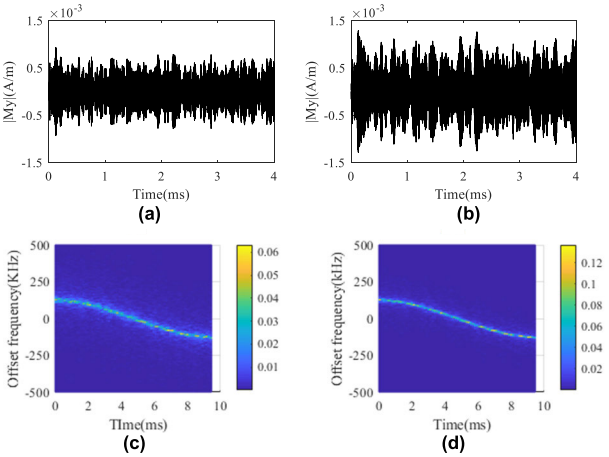

FIGURE 4. Simulation results under longitudinal 50Hz sinusoidal magnetic field: (a) The waveform of magnetization component M_y in the first sample; (b) The waveform of magnetization component M_y in the second sample; (c) The time-frequency diagram of M_y in the first sample; (d) The time-frequency diagram of M_y in the second sample.

III. NSS-NMR EFFECT BASED TVMF MEASURING APPARATUS

A. ARCHITECTURE OF MEASURING APPARATUS

According to the NSS-NMR effect and the accurately known gyromagnetic ratio of spin nuclear magnetic moment (for example, $\gamma_H = 42.57746778$ MHz/T for ^{1}H), the longitudinal

TVMF could be accurately measured by inversion the time-frequency curve of the NSS-NMR signal based on the Larmor precession equation. A set of TVMF measuring apparatus is designed and developed which can deal with not only the NSS-NMR experiment but also the conventional pulsed-NMR experiment under longitudinal TVMF environment. The apparatus includes a magnet which generates the longitudinal TVMF to be measured, a RF excitation transmitting channel, an orthogonal dual-coil probe with enwrapping NMR experimental sample, a directional coupler and attenuator, a dual-channel RF signal receiving-acquisition and real-time storage subsystem, a signal processing and magnetic field inversion subsystem, and a host computer controlling and analysis processing software. The block diagram of the experimental apparatus is shown in the Fig. 5.

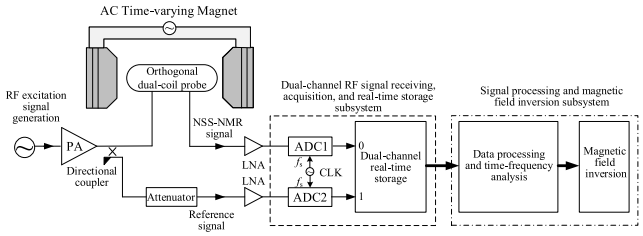

FIGURE 5. The block diagram of the NSS-NMR experimental apparatus under 50 Hz AC modulated mixed magnet environment.

The RF excitation transmitting channel outputs a RF signal with a certain bandwidth and power. The exciting signal is power amplified and then applied to the RF exciting coil of the orthogonal dual-coil probe through the direct output path of the RF wideband directional coupler to generate transverse RF excitation magnetic field in the sphere space (R = 0.5 mm) of the NMR sample with approximately uniform distribution. Under the combined excitation of the longitudinal TVMF and the transverse RF magnetic field, the weak time-varying NSS-NMR signal is excited in the sample and finally generated the NSS-NMR voltage on the probe output port. Being low-noise amplified and filtered, the voltage is acquired by the high-speed and high-precision analog-to-digital converter (ADC) and then stored into a disk-array in real time. The output signal from the coupling port of the directional coupler is attenuated properly and then sampled synchronously by another ADC with distortion free and then stored into the disk-array as a reference signal. The dual-channel acquisition data are processed offline and the time-frequency inversion curve of the longitudinal TVMF is finally obtained.

The measured mixed magnet consists of a permanent magnet (field intensity is 0.579T) and a multi-turn Helmholtz coil connecting to a 50 Hz AC transformer whose output may vary in the range of 0 to 250 V to generate maximum amplitude 3mT sinusoidal magnetic field, so the corresponding Larmor precession frequency varies from 24.526 MHz to 24.782 MHz for ^{1}H nuclear.

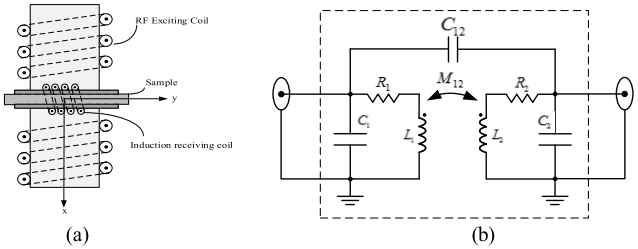

FIGURE 6. The orthogonal dual-coil probe (impedance match circuits not being included): (a) Section view of probe; (b) Lumped parameter equivalent circuit model.

TABLE 1. Parameters extraction results of orthogonal dual-coil equivalent circuit.

Parameters	Self-Inductance (Unit: μH)	Turn Capacitance (Unit: pF)	Ohmic Resistance (Unit: mΩ)	Mutual Inductance (Unit: nH)	Mutual Capacitance (Unit: pF)
Exciting coil	0.2625	1.145	18.7	0.29	0.449
Receiving coil	0.1373	0.491	8.6		

TABLE 2. Variation of some lumped parameters before and after considering the skin effect of the copper wire.

Parameters	Not consider Skin effect		Consider Skin effect	
	Excitation Coil	Induction Coil	Excitation Coil	Induction Coil
self-inductance(μ H)	0.2625	0.1373	0.2588	0.1335
Ohm resistance (mΩ)	18.7	8.6	56.3	27.0
Mutual inductance (nH)	0.29		0.27	

B. ORTHOGONAL DUAL COIL PROBE AND EXTRACTION ITS EQUIVALENT CIRCUIT PARAMETERS

Since excitation spin nuclei resemble and acquisition the NSS-NMR signal must be in progress simultaneously in NSS-NMR experiment, and the RF excitation magnetic field direction (x-axis direction) is perpendicular to the direction of the magnetization component M_y, an orthogonally dual-coil probe is fabricated which includes a RF excitation coil and an induction receiving coil twined orthogonally on the coil skeleton, the NMR experimental sample and the impedance matching circuits. The coil skeleton is made of two perpendicular polyformaldehyde (POM) cylindrical rods with uniform thread grooves etched on the surface, the RF excitation coil and induction coil are then uniformly wound along the grooves with two-section structure to form two solenoid coils with equal turns gap. The axial directions of the RF excitation coil and induction coil are along the x-axis and y-axis respectively, the NMR experimental sample is sealed in a glass tube with 5mm diameter and 7mm length and fixed inside the hole hollowed in the crossbar section of the two POM rods. The NMR sample is saturated copper sulfate solution.

Fig. 6(a) shows the sectional drawing of the orthogonal dual coil. The lumped parameter equivalent circuit model of the orthogonal solenoid dual coils is shown as Fig. 6(b), where L_1 and L_2 are the self-inductances of the excitation coil and induction coil, R_1 and R_2 are the ohmic resistances of the coils, C_1 and C_2 are the turn capacitances of the two coil, C_{12}

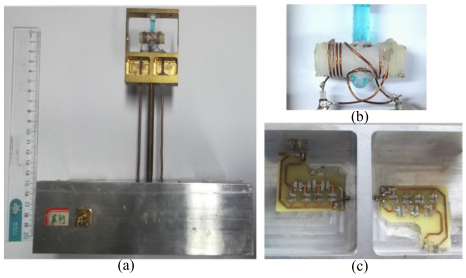

FIGURE 7. Prototype of the orthogonal dual coil probe: (a) Front view; (b) Dual- coil structure with NMR sample enwrapped; (c) Two all-reactance three-stage Π-type broadband matching circuits.

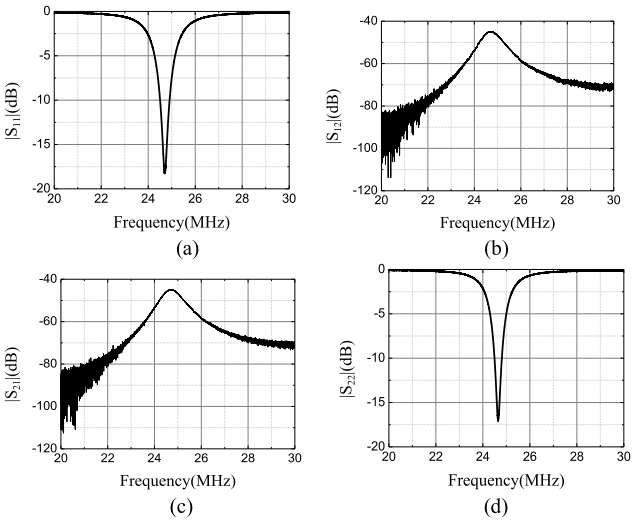

FIGURE 8. Measuring results of the orthogonal dual coil probe: (a) |S11|; (b) |S12|; (c) |S21|; (d) |S22|.

and M_{12} are the mutual capacitance and mutual inductance between the two coils.

The above equivalent circuit parameters could be extracted as following [16]. Firstly, applying constant current or static charge on the turn loops of the two coils, calculating the spatial electric field distribution and magnetic field distribution by the finite element method (FEM) [24], then three-dimensional numerical integrating the electric field energy and magnetic field energy distributed in the region of the whole orthogonal dual-coil structure, finally establishing the linear equations among the field energies and the circuit parameters and then solving the equations to obtain the parameter extraction results which are shown in Table 1.

In order to extract more accurate parameters, the skin effect of RF currents and fields must be considered. Here, the copper wire (diameter D=0.5mm) used to wind the dual coils is emulated as the hollow wires with the thickness equaling to the skin depth [25]. Since the hollow wire minishes the cross-sectional area of the wires, the internal self-inductance and mutual inductance of the coils decrease while the ohmic resistance increases. Table 2 lists the improved extraction results of the inductances and resistances of the coils.

The prototype of the probe is shown in Fig. 7(a). Since the internal space of the magnet being very narrow, the

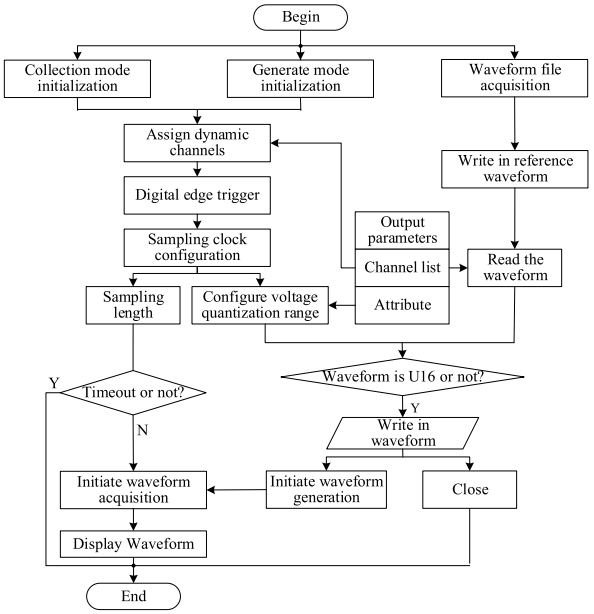

FIGURE 9. Flowchart for generation RF excitation signal using NI-AT1120 arbitrary waveform generator board.

remote three-stage wideband impedance matching circuits being connected to the dual coils by rigid coaxial lines are located outside of the mixed magnet [26], [27]. In order to reduce the electromagnetic field coupling between the two matching circuits, the two matching circuits are fixed in their own shielding boxes to isolate each other.

The measured characteristics of the ports reflecting coefficients and isolation of the probe prototype is shown in Fig. 8. The frequency range of $|S_{11}|$ and $|S_{22}|$ less than -10 dB covers from 24.50MHz to 24.80MHz, $|S_{21}|$ and $|S_{12}|$ are approximately lower than -45dB.

C. RF EXCITATION SIGNAL GENERATION, DUAL-CHANNEL SIGNAL RECEIVING AND PROCESSING

1) RF EXCITATION SIGNAL GENERATION

The RF excitation signal is generated by a NI-AT1120 high-speed arbitrary waveform generator board and power amplified to feed to the signal excitation port of the orthogonal dual coil probe. Firstly, the waveform file is coded and download into the memory of the board. Then a series of parameters, such as sampling length, data width, playback times, data flow mode, are set by the host computer software, finally the waveform data is read out and the RF excitation signal is data-to-analog converted. The overall implementation process is described in Fig. 9.

2) NSS-NMR SIGNAL RECEIVING AND PROCESSING

The dual-channel RF signal receiving, acquisition and real-time storage subsystem is built based on NI PXIe-5122 high-speed digitizer and high-speed disk array. The overall process is shown in Fig. 10(a). Firstly, the dual-channel RF signals from the output port of the probe and the coupling port of the directional coupler are amplified by two large dynamic

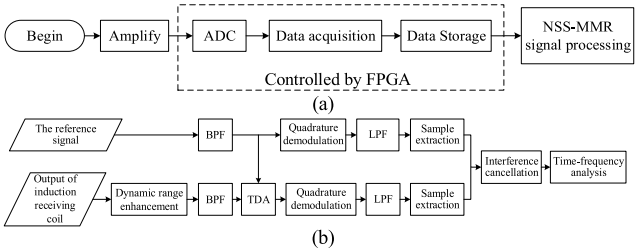

FIGURE 10. Dual-channel signals receiving, acquisition and offline processing: (a) Flowchart of the signal receiving, acquisition and storage in real time; (b) Flowchart of the dual-channel signal processing.

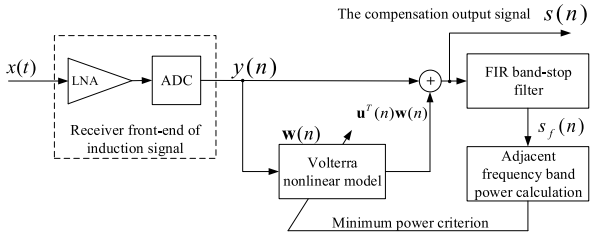

FIGURE 11. Diagram of the nonlinear blind identification and compensation processing algorithm.

range low noise amplifiers respectively, then the signals are sampled by the dual-channel ADC device and storied into the onboard DDR memory or the outside disk array in real time.

Subsequently, the stored dual-channel data are processed offline which include nonlinear distortion compensation, band-pass filtering, time delay alignment, quadrature demodulation, I/Q low-pass filtering and data extraction, adaptive interference cancellation. At the time, the weak transient NSS-NMR signal may be obtained and finally the time-frequency curve can be calculated by the time-frequency analysis techniques to invert the longitudinal magnetic field intensity of the mixed time-varying magnet. Fig. 10(b) shows the above processing flow.

D. SFDR ENHANCEMENT AND INTERFERENCE CANCELLATION

1) SFDR ENHANCEMENT PROCESSING FOR RECEIVER FRONT-END

The receiving and sampling front-end circuits reveal obvious nonlinear distortion under the excitation of strong emission leakage signal. The intermodulation distortion and harmonic distortion components of the front-end could usually not be removed by the conditional bandpass filtering since the components lie in or near the passband of the front-end. We have invented a so-called nonlinear blind identification and compensation technique to deal with the difficulty and improving the spurious-free dynamic range (SFDR) of the receiver front-end [28].

In the technique, a cost function is constructed by "minimizing the power lying in adjacent frequency band" and is used to adaptively iterate out the kernel coefficients of the nonlinear compensation filter corresponding the nonlinear front-end. This is a kind "blind" parameter identification technique since it does not need any information of the input signal. Fig. 11 shows the whole processing diagram of the algorithm where the Volterra series is selected as the nonlinear compensation model of the receiving-sampling front-end.

Assume $x(t)$ being the input signal coming from the orthogonal dual coil probe, which consists of the weak transient NSS-NMR signal, the strong transmit leakage signal and noise. $y(n)$ and $s(n)$ are the output signal of the front-end and the nonlinear compensation output signal, respectively. The FIR band-stop filter is utilized to extract the adjacent band signal to compute the cost function of the nonlinear blind identification. The compensation output signal $s(n)$ is:

$$s(n) = y(n) - \mathbf{u}^{\mathbf{T}}(n)\mathbf{w}(n) \tag{6}$$

where $\mathbf{u}(n)$ is the column vector formed by the each order nonlinear combination terms of the input signal. $\mathbf{w}(n)$ is the column vector formed by the kernel coefficients of the Volterra compensation model, they are as following:

$$\begin{aligned}\mathbf{u}(n) = \Big[&y^2(n), y(n)y(n-1), \ldots, y^2(n-N_d+1),\\ &y^3(n), y^2(n)y(n-1), \ldots, y^D(k-N_d+1)\Big]^T\\ \mathbf{w}(n) = \Big[&\bar{h}(0,0), \bar{h}(0,1), \ldots, \bar{h}(N_2-1, N_2-1), \bar{h}(0,0,0),\\ &\bar{h}(0,0,1), \ldots, \bar{h}(N_{\mathrm{D}}-1, \ldots, N_{\mathrm{D}}-1)\Big]^T\end{aligned}$$

$\bar{h}$ and D are the kernel coefficients and the highest nonlinear order in Volterra series, respectively, N_d is the d-order memory depth of Volterra kernels, and $2 \le d \le \mathrm{D}$ must be met.

The cost function of the blind identification is the short-time energy of the band-stop filtering output signal $s_f(n)$:

$$J(\omega) = \sum_{n=1}^{N} \left[s_f(n)\right]^2 \tag{7}$$

In the duration of each segment of the signal, the Volterra model parameter $\mathbf{w}$ is maintained, so the compensation output signal can be written as a row vector:

$$\mathbf{s}(n) = \mathbf{Y}(n) - \mathbf{U}^{\mathbf{T}}(n)\mathbf{w} \tag{8}$$

where $\boldsymbol{Y}(n) = [y(n), y(n-1), \ldots y(n-M+1)]$, $\mathbf{U}^{\mathbf{T}}(n) = [\mathbf{u}(n), \mathbf{u}(n-1), \ldots \mathbf{u}(n-M+1)]$. So the cost function can be expressed as:

$$\begin{aligned}J(\boldsymbol{w}) = \sum_{n=1}^{N} [&\boldsymbol{Y}^T(n)\boldsymbol{h}\boldsymbol{h}^T\boldsymbol{Y}(n) - \boldsymbol{Y}^T(n)\boldsymbol{h}\boldsymbol{h}^T\boldsymbol{U}^T(n)\boldsymbol{w}(n)\\ &- \boldsymbol{w}^T(n)\boldsymbol{U}^T(n)\boldsymbol{h}\boldsymbol{h}^T\boldsymbol{Y}(n)\\ &+ \boldsymbol{w}^T(n)\boldsymbol{U}^T(n)\boldsymbol{h}\boldsymbol{h}^T\boldsymbol{U}^T(n)\boldsymbol{w}(n)]\end{aligned} \tag{9}$$

So the optimal estimation of the Volterra kernel coefficients is $\hat{\boldsymbol{w}} = \arg\min_{\boldsymbol{w}} J(\boldsymbol{w})$. Applying $\partial J(\boldsymbol{w})/\partial \boldsymbol{w}|_{\boldsymbol{w}=\hat{\boldsymbol{w}}} = 0$ to solve out the estimated parameters $\boldsymbol{w}$:

$$\mathbf{w} = \sum_{n=1}^{N} \frac{\mathbf{U}(n)\mathbf{h}\mathbf{h}^T\mathbf{Y}(n)}{\mathbf{U}(n)\mathbf{h}\mathbf{h}^T\mathbf{U}^T(n)} \tag{10}$$

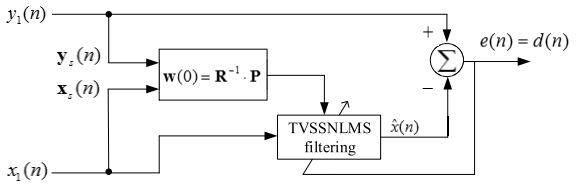

FIGURE 12. Flowchart of the Wiener-TVSSNLMS algorithm.

TABLE 3. Comparison of interference cancellation performances of three algorithms.

SIR of input mixed signal (dB)	SIR of output signal (dB)		
	LMS	TVSSNLMS	Wiener-TVSSNLMS
-10	26.66	32.14	40.72
-20	22.69	25.32	30.92
-30	9.99	15.57	21.05

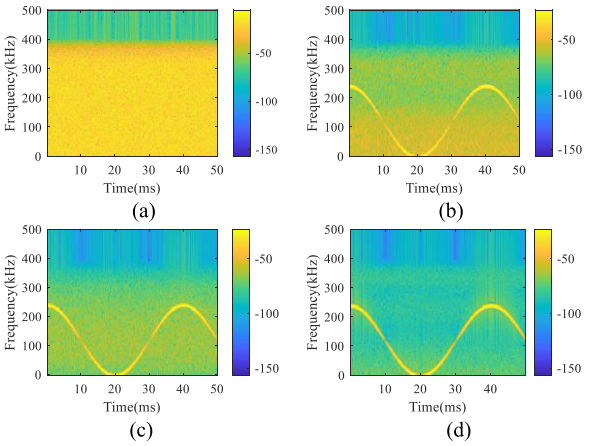

FIGURE 13. Performance comparison of three interference cancellation algorithms: (a) STFT result of the input mixed signal; (b) STFT result of the LMS processing; (c) STFT result of the TVSSNLMS processing; (d) STFT result of the Wiener-TVSSNLMS processing.

2) INTERFERENCE CANCELLATION PROCESSING

Although the isolation between the orthogonal dual coils being high as 45dB, a large part of strong RF excitation signal still leaks into the induction receiving coil. This forms the co-time co-frequency interference to the weak NSS-NMR signal, so some interference cancellation processing must be utilized to improve the signal-to-interference ratio (SIR) of the NSS-NMR signal. A Wiener time-varying step-size normalized least mean square (Wiener-TVSSNLMS) algorithm is proposed and the higher interference cancellation effect without prior knowledge of the transmitting and receiving signals is achieved. The algorithm adjusts the step factor by joint autocorrelation of real-time error signal and time t.

Fig. 12 depicts the flowchart of the algorithm, where the Wiener filtering algorithm being firstly utilized to calculate the initial weight coefficient, then the time-varying step-size least mean square (TVSSLMS) algorithm is applied to adaptively update the weight coefficients, thereby the cancellation effect and the convergence speed could all be improved.

The interference cancellation performances of LMS, TVSSNLMS and Wiener-TVSSNLMS algorithms are compared by processing a cosine envelope frequency modulation complex signal $s(t) = 5\cos(k\pi t)\, e^{j\left[fk^{-1}\sin(2\pi kt)+2\pi ft\right]}$, where $f = 180$ kHz and $k = 25$. The interference signal is band-limited Gaussian distribution signal and the reference signal $x_1(n)$ is obtained from the interference source signal passing through a finite impulse response (FIR) filter. The sampling rate is 1MHz and the sampling time is 50ms.

When the SIR of the input mixed signal are -10 dB, -20 dB, and -30 dB respectively, the SIRs of the interference cancellation output signals are list in Table 3. The results show that the proposed algorithm possesses the best performance and the SIR improvement is about 50dB.

Fig. 13 shows the short-time Fourier transform (STFT) results of the input mixed signal $y_1(n)$ and three processed signal, where SIR of $y_1(n)$ being -30dB. The SIR rises sharply and the frequency of the output signal varies sinusoidally with time can all be observed after interference cancellation processing, especially the Wiener-TVSSNLMS algorithm cancelling the interference most enough.

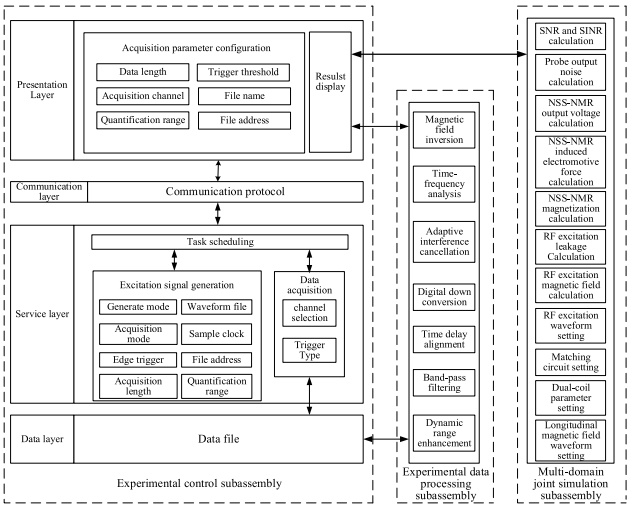

FIGURE 14. The overall logical architecture of the host computer controlling and analysis software.

E. HOST COMPUTER CONTROLLING AND ANALYSIS SOFTWARE

1) SOFTWARE ARCHITECTURE

According to the requirements of the NSS-NMR experiment process, such as the parameter configuration, the RF excitation generation, signal receiving-acquisition-storage, the experimental data processing and the whole NSS-NMR process simulation, the host computer controlling software should include the NSS-NMR experimental control subassembly, the data processing subassembly and CFN-MDJS subassembly. The overall logical architecture of the software is shown in Fig. 14.

The experimental control subassembly includes the presentation layer, communication layer, service layer and data layer. In the presentation layer, the operating parameters is configured and framed and distributed to the other layer.

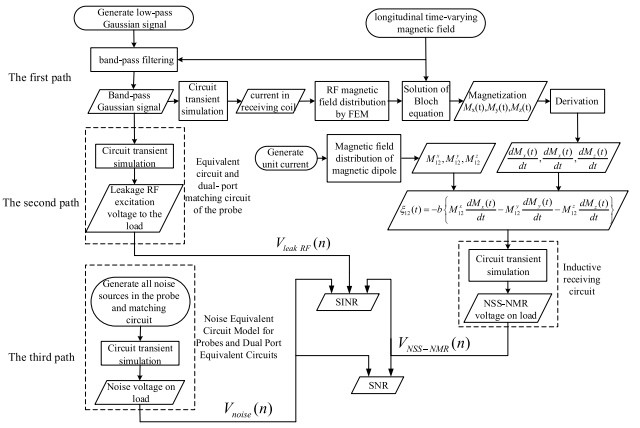

FIGURE 15. Flowchart of the CFN-MDJS.

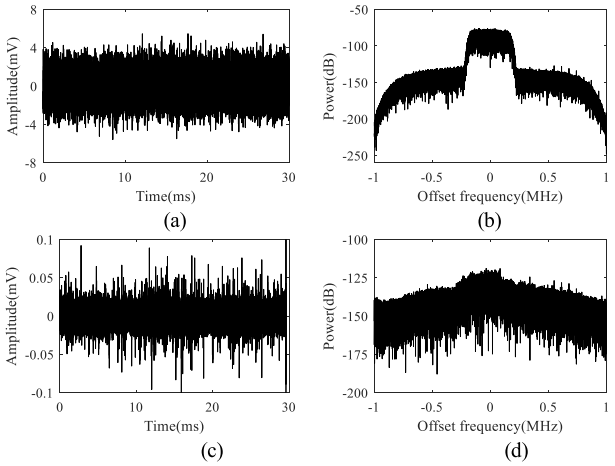

FIGURE 16. Output signal of the inducing coil: (a) Waveform before interference cancellation; (b) Power spectrum before interference cancellation; (c) Waveform after interference cancellation; (d) Power spectrum after interference cancellation.

The communication layer transfers data between the host computer and the physical board and transmits the command frames to the service layer. The AT-1120 board receives data frames coming from upper layer, then parsing and executing the commands, generation the RF excitation signals. At the same time, the NI PXIe-5122 acquisition card synchronously receives the command frame, and acquire the dual-channel output signals. The dual-channel RF data are finally stored for subsequent processing. The other two subassemblies juxtaposed with the experimental control subassembly are the offline data processing unit and the CFN-MDJS unit which the corresponding results are also displayed on the display layer.

2) CFN-MDJS

The CFN-MDJS can emulate the entire process of the NSS-NMR effect and quantitatively evaluate the effectiveness of the signal processing techniques utilized in the experimental apparatus. The CFN-MDJS follows the occurrence sequence of the physical phenomena in the orthogonal dual coil probe and calculates along three paths to obtain the NSS-NMR signal, the leakage RF excitation signal and circuit noise, and finally statistically counts the signal-to-noise ratio (SNR) and signal-to-interference plus noise ratio (SINR) of the NSS-NMR signal.

The first calculation path is to generate a bandpass RF excitation voltage, calculate the current in the RF exciting circuit (consisting of excitation source, matching circuit and excitation coil) by transient simulation technique, calculate the radio frequency magnetic field distribution induced by the RF current flowing through the excitation coil by FEM, numerically solve the Bloch equations by the Runge-Kutta method to obtain the time domain transient longitudinal/transverse magnetization in the spin nuclei sample, calculate the NSS-NMR electromotive force in the inducing coil through the mutual inductance between the magnetic dipole and the coil, calculate the output voltage of the induction receiving circuit (consisting of inducing electromotive force, inducing coil, matching circuit and load) by transient simulation technique.

The second calculation path is to obtain the leakage RF excitation voltage to the output load by the transient simulation technique based on the lumped parameter equivalent circuit and the dual-port matching circuit of the orthogonal dual coil probe.

The third calculation path is to obtain the total output noise voltage at the load by the transient simulation technique based on the noise equivalent circuit model of the probe and the dual-port matching circuit. Fig. 15 shows the processing flowchart of the CFN-MDJS.

The equal length overlapping data segments are partitioned from the NSS-NMR voltage $V_{NSS-NMR}(n)$ sampling sequence, the leakage RF excitation voltage $V_{leak\ RF}(n)$ sequence and the noise $V_{noise}(n)$ sequence at the load to define the SNR and SINR of the NSS-NMR signal as follow,

$$SNR_q = \frac{\sum_{n=1}^{P} \left| V_{NSS-NMR}^{(q)}(n) \right|^2}{\sum_{n=1}^{P} \left| V_{noise}^{(q)}(n) \right|^2}, \quad q = 1, 2, \ldots, Q \tag{11}$$

$$SINR_q = \frac{\sum_{n=1}^{P} \left| V_{NSS-NMR}^{(q)}(n) \right|^2}{\sum_{n=1}^{P} \left\{ \left| V_{leakRF}^{(q)}(n) \right| + \left| V_{noise}^{(q)}(n) \right|^2 \right\}}, \quad q = 1, 2, \ldots, Q \tag{12}$$

where P and Q are the number of points in each segment and all segments.

IV. EXPERIMENTAL RESULTS AND ANALYSIS

A. MEASUREMENT EXPERIMENT UNDER 50 Hz SINUSOIDAL TVMF ENVIRONMENT

The developed NSS-NMR experimental apparatus shown in the Fig. 5 is used to invert the magnetic field intensity of the 50 Hz AC modulated hybrid magnet. The RF excitation magnetic field is generated by the bandpass Gaussian signal

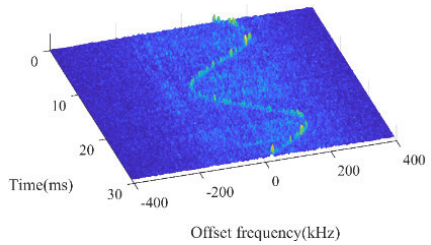

FIGURE 17. Three-dimensional time-frequency diagram of the extracted NSS-NMR signal with the magnetic field inversion experimental apparatus.

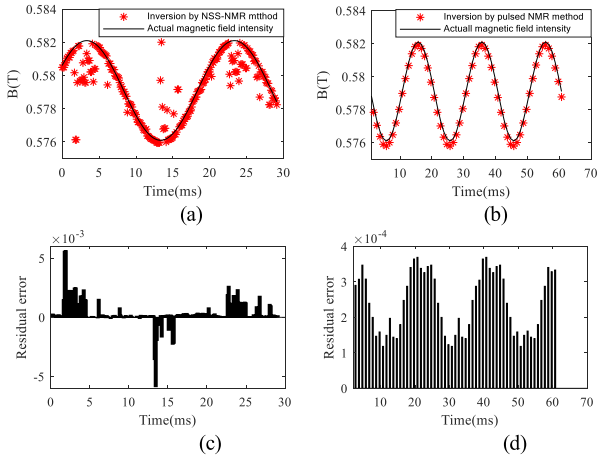

FIGURE 18. Inversion results: (a) The sinusoidal TVMF and the fitting curve by the NSS-NMR method; (b) The sinusoidal TVMF and the fitting curve by the pulsed NMR method; (c) The residual error of magnetic field intensity by the NSS-NMR method; (d) The residual error of magnetic field intensity by the pulsed NMR method.

which its center frequency and bandwidth are 24.66 MHz and 300 kHz respectively to cover the Larmor frequency range of the ^{1}H nucleus corresponding to the magnetic induction intensity variation range of the mixed magnet. The dual-channel signals are acquired synchronously with sampling rate 100 MHz, 14bit quantization bit-width and 50ms single continuous acquisition time length to cover multiple periods of the longitudinal TVMF.

The offline processing mode is utilized to deal with the 30ms time-length data segments of the dual-channel acquisition data by the processing process in Fig. 10(b). After the digital down-conversion and filter extraction, the sampling rate of the dual-channel IQ complex baseband signal has been reduced to 2 MHz which can still cover the bandwidth of the NSS-NMR signal (250kHz). The order of the Wiener filter in the Wiener-TVSSNLMS interference cancellation algorithm is 800 and the first 800 sampling points of the cancellation output should be removed to avoid subsequent time-frequency analysis distortion. Fig. 16 depicts the waveform and power spectrum results before and after the Wiener-TVSSNLMS processing. It shows about 46 dB interference cancellation.

After the interference cancellation processing, the 30ms time-length signal is divided into 228 segments with 1024 sampling points and 75% overlap points in each segment. The windowed Fourier transform is performed on each segment, the three-dimensional short-time Fourier transform time-frequency diagram of the offset frequency of the NMR frequency corresponding to all the segmented data and parameters B_0 is finally obtained (0Hz in the diagram corresponds to the Larmor frequency of the mixed magnet's median magnetic field of 0.579 T at 24.654 MHz), as shown in Fig. 17. A clear sinusoidal waveform could be seen which indicates the existence of the NSS-NMR effect and the weak NSS-NMR signal has been extracted.

The inverted longitudinal TVMF intensity from the above NSS-NMR signal is shown in Fig. 18(a) which the changing range and the period of the TVMF are 0.57595T $\sim$ 0.5820T and 20ms respectively. As a comparison, the inversion result of the TVMF by the conventional pulsed-NMR method is shown as the changing range of 0.57579T $\sim$ 0.58192 T in Fig. 18(b) by setting the pulse width of the RF excitation pulse sequence $\tau \leq 1/\Delta f = 3.91\ \mu s$. These results verifies the credibility of the NSS-NMR inversion result. Fig. 18(c) and (d) show the residual errors of these two measuring methods respectively. Some scatter points deviate from the sinusoidal curve in Fig. 18(c) which may relate to over-cancellation or residual interference of the interference cancellation algorithm.

B. SIMULATION VERIFICATION FOR RF EXCITATION SIGNAL ENVELOPE SHAPING TECHNIQUE

Since the transverse magnetization component $M_x(t)$ and $M_y(t)$ of the NSS-NMR is proportional to the field intensity of the longitudinal TVMF and RF excitation magnetic field, the NSS-NMR magnetization in the initial and end sections of the longitudinal pulsed magnetic field is more weaker than in that in the middle section while the RF excitation signal of smooth Gaussian bandpass signal is applied to the spin nuclei ensembles, also resulting very low SNR in corresponding time duration.

Suppose the longitudinal TVMF is $B_z(t)$, the RF excitation signal is constant envelope signal $s(t)$, the shaping function is $f\,[B_z(t)]$, so the RF excitation signal after envelope shaping changes to $x(t) = s(t) \cdot f\,[B_z(t)]$. Here, some different kinds of shaping functions affecting the SNR of NSS-NMR signal are compared by the CFN-MDJS subassembly.

1) THE SHAPING FUNCTION: $f[B_z(t)] = B_{z,\max}/B_z(t)$

Fig. 19(a) and (b) show the waveform of the longitudinal pulsed magnetic field and the corresponding shaping function curve, respectively. Before envelope shaping, the RF excitation signal is a constant envelope Gaussian bandpass signal with a power of 1W and the frequency range covers from 5.1MHz to 25.5MHz (corresponding to the field intensity of the red dashed line range in Fig. 19(a)). Before and after envelope shaping, the waveforms of the RF excitation signal are shown in Fig. 19(c) and Fig. 19(d), the SNR and SINR of the NSS-NMR signal are listed in Fig. 19(e) to (h), respectively. The SNR is significantly improved and greater than

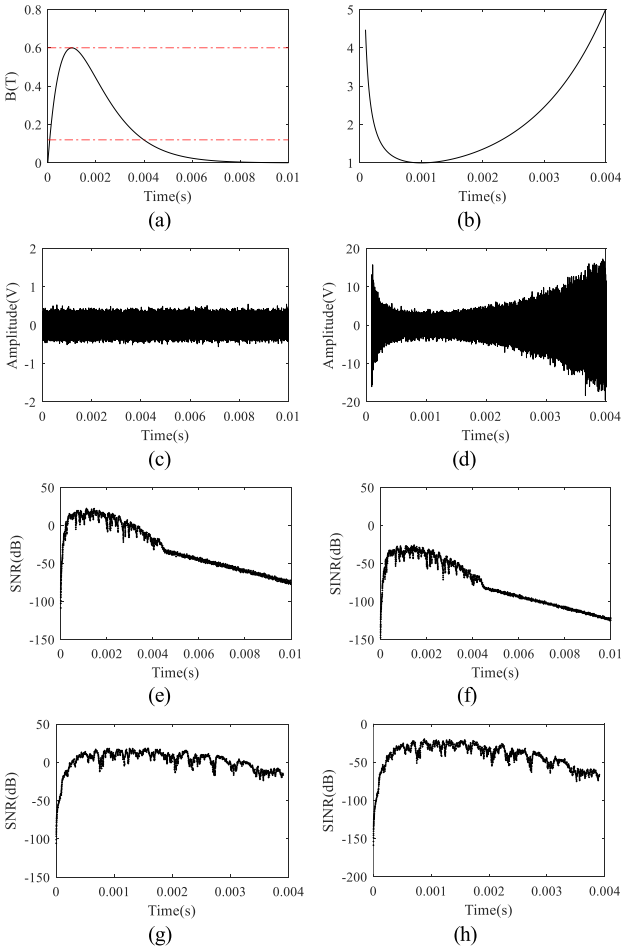

FIGURE 19. Simulation results with the envelope shaping function $f[B_z(t)] = B_{z,\max}/B_z(t)$: (a) Waveform of pulsed magnetic field; (b) Envelope shaping curve; (c) Constant envelope RF Gaussian band-pass signal; (d) RF excitation signal after envelope shaping; (e) SNR before envelope shaping; (f) SINR before envelope shaping; (g) SNR after envelope shaping; (h) SNR after envelope shaping.

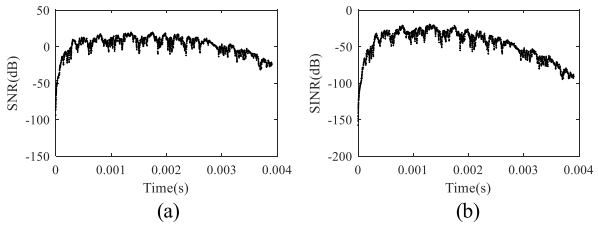

FIGURE 20. Results with the envelope shaping function $f[B_z(t)] = [B_{z,\max}/B_z(t)]^2$: (a) SNR; (b) SINR.

0 dB within a wide time duration by the envelope shaping technique.

2) THE SHAPING FUNCTION: $f[B_z(t)] = [B_{z,\max}/B_z(t)]^2$

In order to more heavy compensation to the low-frequency component of the NSS-NMR response corresponding to low field duration of the pulsed magnetic field, the envelop shaping function can be changed to the square or cubic form. Fig. 20 displays the SNR and SINR curves of the NSS-NMR signal after square shaping application without change of the other experiment parameters. Here the more

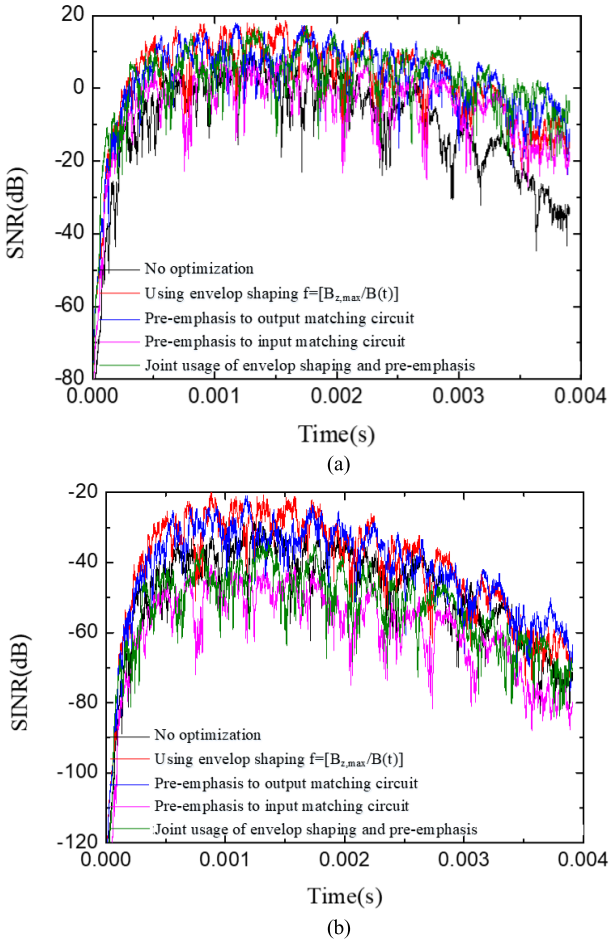

FIGURE 21. Under longitudinal pulsed-magnetic field, the simulation results of applying the RF excitation signal envelope shaping, the matching circuit low frequency pre-emphasis and joint usage of the two techniques: (a) SNR; (b) SINR.

SNR improvement is achieved during the initial section of the pulsed magnetic field.

The above results demonstrate the envelop shaping technique is helpful for improving and smoothing the SNR curve of the NSS-NMR signal duration the whole range of the longitudinal pulsed magnetic field, that provides the basis for subsequent time-frequency analysis and magnetic field inversion. Under the sinusoidal TVMF environment produced by the 50 Hz AC modulated mixed magnet, the SNR enhancement effect could also be achieved with the envelope shaping function being reciprocal of the sinusoidal magnetic field intensity.

C. LOW-FREQUENCY PRE-EMPHASIS WITH RF EXCITATION ENVELOP SHAPING SIMULTANEOUSLY

The dual-port matching circuit low frequency pre-emphasis technique is another effective technique to improve the SNR of the NSS-NMR response, which is also based on the direct proportion between the transverse magnetization components and the longitudinal magnetic field intensity and the RF exciting field. The technique is achieved by adjusting

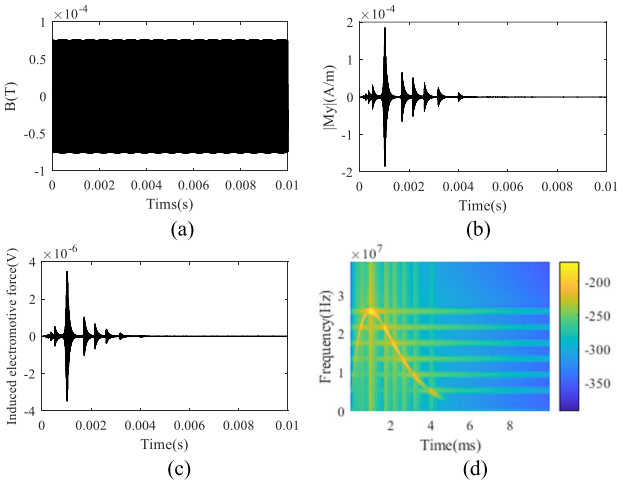

FIGURE 22. The NSS-NMR response excited by a six-tone RF signal with minimum PAPR: (a) The RF excitation magnetic field; (b) The waveform of magnetization My; (c) The waveform of NSS-NMR induced electromotive force; (d) STFT time-frequency diagram of the NSS-NMR signal.

low-frequency band response characteristics of the dual-coil matching circuits. Enhancing the low band responses of the input and output match circuit can improve the RF excitation field intensity and the RF inducing current simultaneously.

Under the longitudinal pulsed magnetic field environment, the RF excitation signal envelope shaping and low-frequency pre-emphasis techniques are adopted simultaneously to observe the SNR and SINR improvement of the NSS-NMR signal. The simulation results by the CFN-MDJS subassembly are depicted in Fig. 21. Here, the resonant frequency of the input/output match circuits are shifted from 24.66MHz to 10MHz to achieve the low-frequency pre-emphasis. The joint usage of the two techniques can decrease the un-flatness of the SNR curve from 26dB to 12dB in the time duration from 0.45ms to 3.25ms. Though the flatness of the SINR curve is not significantly improved since more leakage of the RF excitation signal is transferred to the terminal load, the interference cancellation technique could deal with the situation.

D. SIMULATION VERIFICATION OF DISCRETE MULTI-TONE RF EXCITATION SIGNAL IN NSS-NMR

According to the section II, the magnetization is related to the longitudinal magnetic field and the type of RF excitation signal, so different RF excitation signals excite different magnetization vector. The discrete multi-tone signal is composed of multiple different frequency sinusoidal signals whose peak-to-average power ratio (PAPR) is one of important parameters. High PARA may easily cause the power amplifier or the receiving-acquisition subsystem entering nonlinear even saturation condition to deteriorate the characteristic of the interference cancellation unit. Some techniques may be used to decrease the PAPR of the multi-tone signal. For example, a discrete six-tone signal including 5.11 MHz, 9.20 MHz, 13.29 MHz, 17.38 MHz, 21.47 MHz and 25.56 MHz components is generated with the initial phase equation which the initial phase of the n-th tone meets the following:

$$\varphi_n = \begin{cases} \frac{\pi}{N} n^2; & n \text{ is even number} \\ \frac{\pi}{N} n(n+1); & n \text{ is odd number} \end{cases} \tag{13}$$

Fig. 22 shows the simulation results of the NSS-NMR response under the longitudinal pulsed-magnetic field and the six-tone RF signal. The clearcut FID signals appear at each excitation frequency relevant to the intensity of the longitudinal pulse magnetic field. The phenomena indicates the whole NSS-NMR process is very similar to that of the conventional pulsed-NMR at the situation. Comparison with the continuous spectrum RF excitation signal, the energy of the multi-tone RF signal is concentrated on finite frequency components and is beneficial for improving the excitation efficiency of NSS-NMR signal. As showing in Fig. 22(d), the NMR spectrum peak at lower frequency is still very obvious.

V. CONCLUSION

A new NSS-NMR effect based TVMF measurement method and experimental apparatus are proposed and researched in the paper. The NSS-NMR effect and its principle are derived by extending the Bloch equations and the Larmor precession relationship under constant longitudinal magnetic field to longitudinal TVMF. At the same time, the invented CFN-MDJS subassembly is integrated in the host computer controlling and analysis software. Two kinds of SNR optimization techniques, the RF excitation signal envelope shaping and the low-frequency pre-emphasis matching are proposed and verified by the CFN-MDJS. As another kind type of RF excitation signal, the discrete multi-tone RF signal is also proposed to apply in the NSS-NMR experiment. The inversion results of the 50Hz longitudinal sinusoidal TVMF indicates the NSS-NMR effect and principle are correct and can be experimentally verified. Simultaneously, the proposed apparatus can also utilize to carry out conventional pulsed-NMR experiment.

The next step is to enlarge the frequency bandwidth of the dual-coil matching circuits and improve the physical isolation of the dual coils to meet the experimental requirements under high pulsed magnetic field environment.

REFERENCES

[1] X. Wang, M. Zhu, K. Xiao, J. Guo, and L. Wang, "Static weak magnetic field measurements based on low-field nuclear magnetic resonance," *J. Magn. Reson.*, vol. 307, Oct. 2019, Art. no. 106580.

[2] Z. Frait and D. Fraitová, "Measurement of magnetic field intensity by means of NMR. I. Accuracy of measurement," *Czechoslovak J. Phys.*, vol. 27, no. 11, pp. 1292–1305, Nov. 1977.

[3] S. Zou, H. Zhang, X.-Y. Chen, and J.-C. Fang, "In-situ triaxial residual magnetic field measurement based on optically-detected electron paramagnetic resonance of spin-polarized potassium," *Measurement*, vol. 187, Jan. 2022, Art. no. 110338.

[4] T. Oida, Y. Ito, K. Kamada, and T. Kobayashi, "Detecting rotating magnetic fields using optically pumped atomic magnetometers for measuring ultra-low-field magnetic resonance signals," *J. Magn. Reson.*, vol. 217, pp. 6–9, Apr. 2012.

[5] B. Meier, S. Greiser, J. Haase, T. Herrmannsdörfer, F. Wolff-Fabris, and J. Wosnitza, "NMR signal averaging in 62T pulsed fields," *J. Magn. Reson.*, vol. 210, no. 1, pp. 1–6, May 2011.

[6] L. E. Switala, B. E. Black, C. A. Mercovich, A. Seshadri, and J. P. Hornak, "An electron paramagnetic resonance mobile universal surface explorer," *J. Magn. Reson.*, vol. 285, pp. 18–25, Dec. 2017.
[7] A. W. Kittell, T. G. Camenisch, J. J. Ratke, J. W. Sidabras, and J. S. Hyde, "Detection of undistorted continuous wave (CW) electron paramagnetic resonance (EPR) spectra with non-adiabatic rapid sweep (NARS) of the magnetic field," *J. Magn. Reson.*, vol. 211, no. 2, pp. 228–233, Aug. 2011.
[8] M. E. West, E. L. Sesti, M. M. Willmering, D. D. Wheeler, Z. L. Ma, and S. E. Hayes, "Describing angular momentum conventions in circularly polarized optically pumped NMR in GaAs and CdTe," *J. Magn. Reson.*, vol. 327, Jun. 2021, Art. no. 106980.
[9] N. De Zanche, C. Barmet, J. A. Nordmeyer-Massner, and K. P. Pruessmann, "NMR probes for measuring magnetic fields and field dynamics in MR systems," *Magn. Reson. Med.*, vol. 60, no. 1, pp. 176–186, Jun. 2008.
[10] H. Stork, P. Bontemps, and G. L. J. A. Rikken, "NMR in pulsed high-field magnets and application to high-TC superconductors," *J. Magn. Reson.*, vol. 234, pp. 30–34, Sep. 2013.
[11] J. Haase, D. Eckert, H. Siegel, H. Eschrig, K. H. Müller, and F. Steglich, "High-field NMR in pulsed magnets," *Solid State Nucl. Magn. Reson.*, vol. 23, no. 4, pp. 263–265, Jun. 2003.
[12] J. Haase, D. Eckert, H. Siegel, H. Eschrig, K.-H. Müller, A. Simon, and F. Steglich, "NMR at the frontier of pulsed high field magnets," *Phys. B, Condens. Matter*, vols. 346–347, pp. 514–518, Apr. 2004.
[13] W. Chen, H. Ma, and D. Yu, "Broadband continuous nuclear magnetic resonance signal in a pulsed magnetic field: Numerical solutions of bloch equations under radio frequency irradiation," *Appl. Magn. Reson.*, vol. 47, no. 1, pp. 41–52, Jan. 2016.
[14] W. Chen, H. Ma, D. Yu, and H. Zhang, "SVD-based technique for interference cancellation and noise reduction in NMR measurement of time-dependent magnetic fields," *Sensors*, vol. 16, no. 3, p. 323, Mar. 2016.
[15] W.-J. Chen, H. Ma, D. Yu, and X.-H. Zeng, "Numerical solution to the bloch equations: Paramagnetic solutions under wideband continuous radio frequency irradiation in a pulsed magnetic field," *Chin. Phys. C*, vol. 40, no. 8, Aug. 2016, Art. no. 088201.
[16] X. Zeng, H. Ma, J. Jin, H. Zhang, and J. Ma, "Non-steady state NMR effect and application on time-varying magnetic field measurement," *Sensors*, vol. 22, no. 24, p. 9960, Dec. 2022.
[17] Y. Hu, H. Ma, J. Li, and B. Xu, "The spin transition and susceptibility of NMR samples in a time dependent longitudinal field," *J. Modern Phys.*, vol. 3, no. 11, pp. 1732–1736, 2012.
[18] Y. F. Hu, H. Ma, J. B. Li, and B. Xu, "A study of magnetic susceptibility of NMR samples in a time dependent longitudinal field," *Adv. Mater. Res.*, vol. 629, pp. 911–914, Dec. 2012.
[19] Y. -F. Hu, H. Ma, J. -B. Li, and B. Xu, "Fundamental study on the NMR spectroscopy in a time dependent longitudinal field," presented at the 3rd Int. Conf. Mater. Sci. Inf. Technol., Nanjing, China, 2013.
[20] F. Bloch, W. Hansen, and M. Packard, "Nuclear resonance," *Phys. Rev.*, vol. 70, no. 7, p. 8, 1946.
[21] W. M. Dougherty, K. J. Bruland, S. H. Chao, J. L. Garbini, S. E. Jensen, and J. A. Sidles, "The bloch equations in high-gradient magnetic resonance force microscopy: Theory and experiment," *J. Magn. Reson.*, vol. 143, no. 1, pp. 106–119, Mar. 2000.
[22] A. Abragam and L. C. Hebel, "The principles of nuclear magnetism," *Amer. J. Phys.*, vol. 29, no. 12, pp. 860–861, Dec. 1961.
[23] N. Bloembergen and L. O. Morgan, "Proton relaxation times in paramagnetic solutions. Effects of electron spin relaxation," *J. Chem. Phys.*, vol. 34, no. 3, pp. 842–850, Mar. 1961.
[24] X. Liu, Y. Wang, J. Zhu, Y. Guo, G. Lei, and C. Liu, "Calculation of capacitance in high-frequency transformer windings," *IEEE Trans. Magn.*, vol. 52, no. 7, pp. 1–4, Jul. 2016.
[25] M. Chari and Z. Csendes, "Finite element analysis of the skin effect in current carrying conductors," *IEEE Trans. Magn.*, vol. MAG-13, no. 5, pp. 1125–1127, Sep. 1977.
[26] V. D. Kodibagkar and M. S. Conradi, "Remote tuning of NMR probe circuits," *J. Magn. Reson.*, vol. 144, no. 1, pp. 53–57, May 2000.
[27] D. M. Pozar, *Microwave Engineering*, 3rd ed. New York, NY, USA: Wiley, 2004, pp. 209–216.
[28] L. Peng and H. Ma, "Design and implementation of software-defined radio receiver based on blind nonlinear system identification and compensation," *IEEE Trans. Circuits Syst. I, Reg. Papers*, vol. 58, no. 11, pp. 2776–2789, Nov. 2011.

HANG XU received the B.Sc. degree from Huazhong University of Science and Technology (HUST), Wuhan, China, in 2012, and the M.Sc. degree from Wuhan Institute of Posts and Telecommunications, Wuhan, in 2015. He is currently pursuing the Ph.D. degree with the School of Physics, HUST.

His current research interests include signal processing, NSS-NMR, passive detection, and location.

HONG MA received the B.Sc., M.Sc., and Ph.D. degrees in electromagnetic field and microwave technology from HUST, in 1988, 1992, and 1998, respectively.

He is currently a Professor with the School of Electronic Information and Communications (EIC) and the School of Physics, HUST. His current research interests include NSS-NMR, signal processing, RF and microwave systems, antenna, passive detection and location, spectrum monitoring, and gravitational wave detection.

XIAOHU ZENG received the B.Sc. degree in electromagnetic field and microwave technology from the Communication Command College, Wuhan, China, in 2008, the M.Sc. degree in electromagnetic field and microwave technology from Huaqiao University, Xiamen, China, in 2012, and the Ph.D. degree in electromagnetic field and microwave technology from HUST, in 2023.

His current research interests include NSS-NMR and antenna.

HUA ZHANG received the Ph.D. degree in information and communication engineering from HUST, in 2011.

He is currently an Associate Professor of EIC with HUST. His current research interests include spectrum monitoring, software radio, and gravitational wave detection.

JIANG JIN received the Ph.D. degree in Information and communication engineering from HUST, in 2006.

He is currently an Associate Professor of EIC with HUST. His current research interests include communication, signal processing, passive detection, and location.